

Article

# Numerical and Experimental Investigation of the Heat Input Effect on the Mechanical Properties and Microstructure of Dissimilar Weld Joints of 690-MPa QT and TMCP Steel

Francois Njock Bayock <sup>1,\*</sup>, Paul Kah <sup>1</sup>, Pavel Layus <sup>1</sup> and Victor Karkhin <sup>2</sup>

<sup>1</sup> Laboratory of Welding Technology, Lappeenranta University of Technology, P.O. Box 20, 53851 Lappeenranta, Finland; paul.kah@lut.fi (P.K.); pavel.layus@lut.fi (P.L.)

<sup>2</sup> Welding and Laser Technologies Laboratory, Peter the Great St. Petersburg Polytechnic University, 195251 St. Petersburg, Russia; victor.karkhin@mail.ru

\* Correspondence: francois.njock.bayock@lut.fi; Tel.: +358-46526-7492

Received: 12 February 2019; Accepted: 15 March 2019; Published: 20 March 2019



**Abstract:** The study evaluates numerically and experimentally the effect of welding heat input parameters on the microstructure and hardness of the heat-affected zone (HAZ) of quenched and tempered (QT) and thermo-mechanically controlled process (TMCP) 690-MPa high-strength steel. Numerical analyses and experimental comparisons were applied using three heat input values (10, 14, and 17 kJ/cm) in order to predict the thermal fields during welding. Experimental analysis was carried out of the microstructure and microhardness behavior in different HAZ areas. The numerical values indicate that the maximum respective values of temperature measured in QT steel and TMCP steel were about 1300 and 1200 °C for a heat input of 10 kJ/cm, 1400 and 1300 °C for a heat input of 14 kJ/cm, and 1600 and 1450 °C for a heat input of 17 kJ/cm. The cooling times resulted, for a heat input of 10 kJ/cm, in numerical  $t_{8/5}$  (14.5 s) and experimental (18.84 s) increases in hardness in the coarse-grain heat-affected zone (CGHAZ) of the QT steel (317 HV0.1), due to the formation of bainite and lath martensite structures with grain growth. Decreased hardness in the CGHAZ of TMCP steel (240 HV0.1) was caused by primary recrystallization of the microstructure and the formation of more equilibrium products of austenite decomposition. Increasing the heat input (14 to 17 kJ/cm) led to numerical  $t_{8/5}$  (29 s) and experimental (36 s) decreases in hardness in the CGHAZ of QT steel (270 HV0.1) due to the full austenite (thermal weld cycle), and maintained the relative value of TMCP steel (235 HV0.1).

**Keywords:** thermo-mechanically controlled process steel; quenched and tempered steel; microstructure

## 1. Introduction

High-strength steel (HSS) is used more and more today in almost all industrial fields. The benefits are enormous in terms of tensile strength and elongation, depending on the area of use. It is often essential to understand the microstructural behavior of materials subjected to dissimilar welds. It would be crucial to know the methods of manufacturing the elements and their uses to begin the analysis of their weldability. The weldability of these materials depends on many parameters such as the geometry of the weld joint, and the mechanical and chemical properties of the different elements [1–3]. After that, the characteristics of the filler metal are used when welding with an electric arc or others. In this analysis, two types of HSS are studied, with the same mechanical properties, but of varied chemical composition and a different method of manufacture—quenching and tempering (QT), and thermo-mechanically controlled processing (TMCP). The first stage of QT steel production is hot-rolling with air-cooling,

followed by reheating above the transformation temperature  $AC_3$ , and then water quenching. High cooling rates suppress diffusion-controlled ferrite and pearlite formation and lead to the creation of the main martensite. Subsequent tempering allows the desired mechanical qualities to be achieved by relieving internal stresses [4–7]. The conditions of the thermomechanical rolling in TMCP steel production depend on the plate thickness and chemical composition of the steel being treated. A high degree of deformation in the temperature range of the suppressed recrystallization ( $T_{max} \geq 1150$  °C) results in essential grain refinement of the final microstructure [8,9]. Steel grades with the same value of yield stress (690 MPa) can have significantly different chemical composition. Therefore, the weld joint and the heat-affected zone (HAZ) microstructural and mechanical properties may also differ. The mechanical behavior of the HAZ largely determines the serviceability of a weld joint. Thus, the analysis of the mechanical behavior and the microstructure of dissimilar high-strength steels reveals a particular interest in the field of current research [10–12]. Researchers usually give primary attention to the coarse-grain region of the HAZ (CGHAZ), which is traditionally considered the most unfavorable area of the HAZ. However, such a consideration is not always valid. For example, some areas of the HAZ can contain a relatively soft layer with under-matched mechanical properties, and it is, thus, essential to assess the features of the entire HAZ [13,14]. Successful welding of HSS requires a thorough understanding of microstructural transformations and other phenomena occurring during and after the welding process. A correctly chosen welding heat input will result in a high-quality weld without induced cold cracking and stress corrosion cracking defects, which are often observed in the CGHAZ region [15–17]. In the case of multi-pass welding, deterioration of toughness can be caused by small areas of poor fracture toughness, referred to as local brittle zones. This zone is often situated between the interconnection of two weld passes in CGHAZ [18]. Some authors [19–22] evaluated the mechanical properties (tensile strength, impact energy, and crack opening displacement) in consumable electrode arc welding of QT and TMCP steels. Their results indicated that the tensile strength is higher than 800 MPa [22]. However, they seemed to not consider the effect of the microstructural gradient and the impact of different microhardness in the various HAZ regions. As a result, researchers studied the tensile properties of undermatch welds of QT HSS RQT701 for different heat inputs [23]. It was observed that an increase in the heat input values produces a coarsening of the microstructure of the weld metal (WM) and the HAZ. This microstructure change, in turn, promotes the formation and coarsening of upper bainite in the zones mentioned above with the appearance of some ferrite side plates. Generally, most of the research in this area was conducted without paying attention to microstructural behavior in the different regions of the HAZ [24,25]. In welding simulation, there is an interaction of some disciplines in the physical analysis: the interaction between temperature, mechanical response (residual stress, gap opening, distortion, and hardness), and microstructure (composition, morphology, and chemical reactions). From the analysis of the thermal behavior of the weld joint to the microstructural analysis, there are two phases of heat exchange: the heating phase and the cooling phase. For a numerical analysis of this process, the model using the finite element method can develop the transient heat transfer process. The chemical reactions of materials creating latent heat may be neglected during the process of welding modeling. Goldak [26] modeled the welding simulation using finite element method information to model heat flow as ellipsoidal and double-ellipsoid models. In this study, the values of heat source were applied in the weld joint of two base materials. The numerical analyses of heat source were carried out on the diffusion in the weld joint. Then, thermal conduction was observed from the weld joint to the different base materials. The cooling time ( $t_{8/5}$ ) of each welding operation enabled us to evaluate the different microstructure behavior (grain size) and the mechanical strains (microhardness results). A comparative thermal profile (numerical and experimental) was performed in order to predict the reasonable cooling time and hardness susceptible to having a great morphology of the microstructure in the different HAZ regions (fine-grain HAZ (FGHAZ) and GHAZ).

## 2. Materials and Methods

The analyses were conducted on two types of HSS with the same tensile strength of 690 MPa (QT and TMCP). Table 1 represents the chemical composition of the base materials used in this experimental analysis. Figure 1 shows the geometry of the weld joint with dimensions 150 mm × 50 mm × 8 mm, equipped with a weld joint having a V-groove butt joint with an angle of 60°, and a 2 mm gap. Table 2 shows the mechanical properties (yield strength, tensile strength, and elongation) of both base materials and filler material. On the basis of the chemical compositions of the different materials, the carbon equivalence values were determined. The mechanical characteristics of the base materials made it possible to determine the characteristics of required weld metal, allowing the application of the different heat inputs requested in this analysis.

The weld applied in this analysis was Gas metal arc welding (GMAW), using shielding gas Ar + 18% CO<sub>2</sub>, and an automatic robotic system. The digital laser system automatically read the thermal transfer (Figure 2a) from the weld metal line to the base materials. This reading by the laser made it possible to determine the temperatures point by point, and it was possible to evaluate the cooling time which from 800 to 500 °C ( $t_{8/5}$ ). The welding parameters were integrated into the central unit, which was interconnected with the servo controller of the robot system and the power source. The welded parts were placed in a cabinet at both ends, and the variations of the heat source automatically changed the speed of the welding process (Figure 2b). Table 3 presents the different parameters applied to the heat source. As the welding used two layers, the first one remained constant at a value of 10 kJ/cm, while the second layer varied; this allowed us to determine the variations of the  $t_{8/5}$  time on the different samples. The weld metal was undermatched, and the yield strength of the filler metal was 72% of that of the base metal. The welding conditions are presented in Table 3. The heat input corresponds to an arc efficiency according to ISO 15614-1:2017.

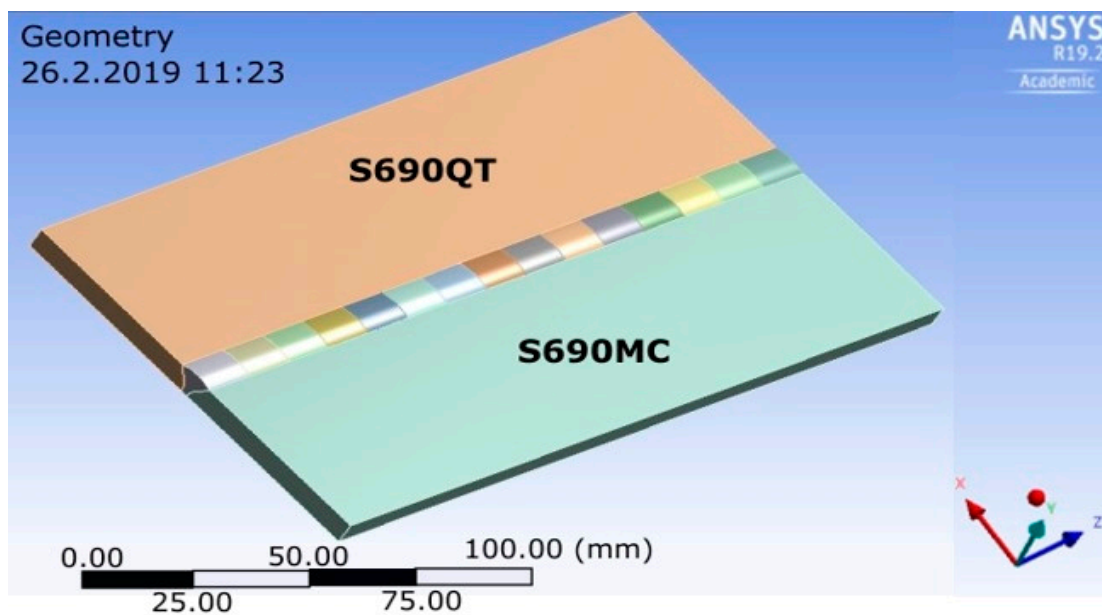


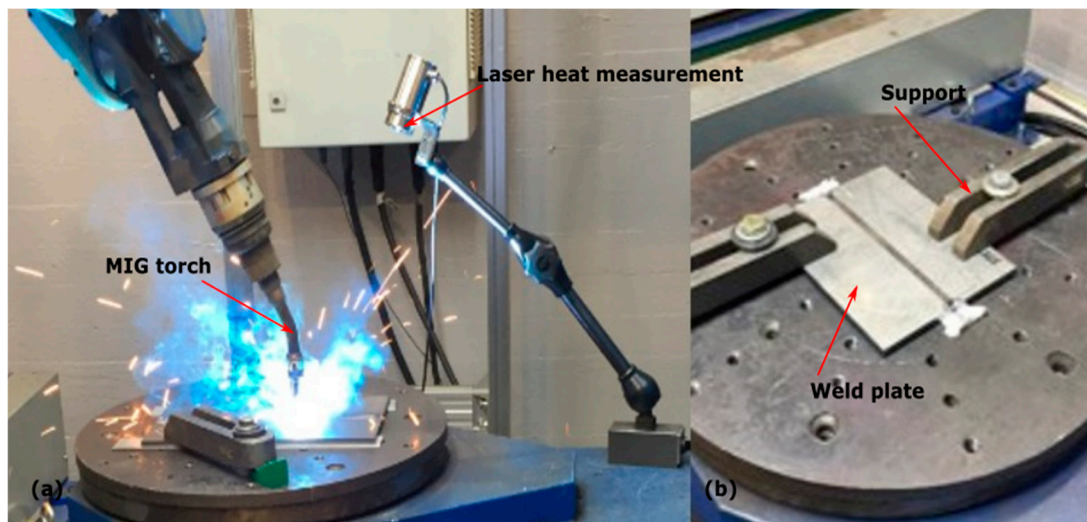
Figure 1. The geometry of the sample.

**Table 1.** The chemical composition of the quenching and tempering (QT), thermo-mechanically controlled process (TMCP) steels, welding wire (wt.%), and the carbon equivalent (CE).

Steel	C	Si	Mn	Al	B	Nb	Ti	V	Cu	Cr	Ni	Mo	N	P	S	CE
QT	0.137	0.28	1.39	0.061	0.0021	0.022	0.002	0.001	0.02	0.062	0.066	0.029	0.005	0.013	0.0013	0.41
TMCP	0.049	0.17	1.86	0.025	-	0.081	0.092	0.009	-	-	-	0.008	0.005	0.08	0.004	0.35
16834-A G 69 6 M21 Mn4ni1,5CrMo	0.07	0.50	1.70	-	-	-	0.05	-	≤0.30	0.20	1,60	0,45	0.005	0.012	0.02	0,55

**Table 2.** Mechanical properties of the steels and welding wire.

Steel	Yield Strength (MPa)	Tensile Strength (MPa)	Elongation A5 (%)
QT	793	835	16.3
TMCP	761	821	20
16834-A G 69 6 M21 Mn4ni1,5CrMo	720	780	≥17

**Figure 2.** Gas metal arc welding process: (a) weld torch and laser heat control; (b) workpiece position.**Table 3.** Welding conditions.

No.	Pass	Current (A)	Voltage (V)	Welding Speed (cm/min)	Net Power (W)	Heat Input (kJ/cm)
1	1	230	25.6	27.18	4710	10
	2	230	25.6	27.18	4710	10
2	1	230	25.6	27.18	4710	10
	2	268	29.0	27.12	6218	14
3	1	230	25.6	27.18	4710	10
	2	258	30.6	22.26	6316	17

The microstructure of the joints was revealed by etching the specimens in an initial etchant (4% solution of HNO<sub>3</sub> in ethanol). The microstructure was examined using a Leica DMI5000M light metallographic microscope (Leica Microsystems, Wetzlar, Germany) with magnification up to 1000×. Image analysis was used for accurate determination of grain size according to ASTM E112-13. Hardness measurements according to ISO 6507-1:2018 were conducted with a Wilson Wolpert 452SVD Vickers hardness tester (ITW, Chicago, IL, USA). The microhardness of single phases was measured by a Wilson Wolpert 402MVD microhardness tester (ITW, Chicago, IL, USA) with a diamond pyramid indenter under a load of 0.0025 N. Evaluation of the grain size was made possible by ImageJ software (ImageJ 2013, NIH, Bethesda, MD, USA). Measurements were taken on samples of FGHAZ from the two base materials. The measurements were automatically performed using ImageJ surface area. Table 1 shows the mechanical properties of the different base materials, while Table 2 shows the chemical composition of QT S690 and TMCP S690 steel.

### 3. Numerical Formulations

In this study, the transient method of heat transfer from the melting point to the base material was applied. The ambient temperature was evaluated at 28 °C. The displacement of the heat source was measured from the thermal diffusion (weld torch) to the weld joint, and from the weld joint to the base material. In this study, flux production was considered constant in its geometry and intensity.  $Q$  ( $W/mm^3$ ), the thermal energy due to the thermal conduction, was analyzed along of the weld joint and was evaluated according to the thermomechanical parameters of each material, i.e., the effect of the thermal conduction on different surfaces of the weld joint.

The heat of the welding arc and molten metal droplets can be considered during the welding process, and the elements representing filler elements in the finite element model are provided in terms of heat input as volumetric and surface heat flux with uniform density. The volumetric heat input  $q$  ( $\frac{W}{mm^3}$ ) is determined by Equation (1).

$$q = \frac{\eta UI}{V} b_v + \frac{\eta UI}{A} b_A, \quad (1)$$

where  $\eta$  is the arc efficiency, and it was assumed to be 0, 90 for GMAW in this study,  $U$  and  $I$  are the arc voltage (V) and welding current (A), respectively, and  $V$ ,  $A$  the different volume ( $mm^3$ ) of elements representing the weld filler material in the finite element (FE) model. In Equation (1), the volumetric heat factors  $b_v$  and  $b_A$  have no physical interpretation. They are only used to fine-tune the heat flux such that the desired fusion zone and temperature distributions can be archived. The conduction in  $x$ -,  $y$ -, and  $z$ -directions for an orthotropic heat conduction model is given in Equation (2) based on Fourier's law of conduction.

$$\left( \frac{\partial}{\partial x} \left[ k_x \frac{\partial T}{\partial x} \right] + \frac{\partial}{\partial y} \left[ k_y \frac{\partial T}{\partial y} \right] + \frac{\partial}{\partial z} \left[ k_z \frac{\partial T}{\partial z} \right] \right) + \dot{q} = \rho c \frac{\partial T}{\partial t}, \quad (2)$$

where  $k_x$ ,  $k_y$ , and  $k_z$  are the thermal conductivity values ( $W/m \cdot ^\circ C$ ) in the  $x$ -,  $y$ -, and  $z$ -directions,  $T(x, y, z)$  is the temperature, and  $x$ ,  $y$ , and  $z$  represent the welding directions in longitudinal, transverse, and thickness directions. The essential boundary was defined as shown in Equation (3).

$$k \frac{\partial T}{\partial x} l_x + k \frac{\partial T}{\partial y} l_y + k \frac{\partial T}{\partial z} l_z + q_z + h_{conv}(T_s - T_0) + \sigma \epsilon (T_s^4 - T_0^4) = 0, \quad (3)$$

where,  $l_x$ ,  $l_y$ , and  $l_z$  are the direction cosines of the outward drawn normal to the boundary,  $h_{conv}$  is the heat transfer coefficient,  $q_z$  is the boundary heat flux,  $\epsilon$  is emissivity whose value was considered as 0.03, and  $\sigma = 5.67 \times 10^{-8} W/m^2 \cdot ^\circ C$  is the Stefan–Boltzmann constant. By applying the finite element method for the resolution of the system, Equation (3) was developed according to the model Galerkin's virtual development of the temperature flow according to Equation (4).

$$\int_v \left( \frac{1}{2} \right) \left[ K_x \frac{\delta^2 T}{\delta x^2} + K_y \frac{\delta^2 T}{\delta y^2} + K_z \frac{\delta^2 T}{\delta z^2} \right] - 2 \left( Q - \rho c \left[ \frac{\delta T}{\delta t} \right] \right) dv + \int_{s_1} q T ds + \frac{1}{2} \int_{s_2} h (T - T_\alpha)^2 ds = 0, \quad (4)$$

where, in the first integral, the first three terms give the thermal stiffness matrix due to conduction,  $[K_{cond}]$ ,  $Q$  gives the body internal heat generated, such as the heat vector,  $\{Q_{body}\}$ , and the last term gives the body heat capacity matrix,  $[C]$ , in terms of the time derivatives of temperature. The second integral gives the thermal load due to heat flux on the surface  $q$ . The first term in the third integral gives the convective load due to the film coefficient  $\{h\}$ . Finally, the stiffness matrix is given in Equation (5).

$$[K] + [K_{cond}] + [K_{conv}]. \quad (5)$$

Moreover, the load vector is defined in Equation (6).

$$\{Q\} + \{Q_{body}\} + \{q\} + \{h\}. \quad (6)$$

The heat energy equations were written in tensor form, whereby the element transient heat equation was obtained and later summed to get the system equation analyzed with time. Equation (7) shows the derived matrix.

$$[K(T)]\{T\} + [(T)]\left\{\frac{\partial T}{\partial t}\right\} = \{Q(T)\}. \quad (7)$$

The finite element model dimensions of a weld specimen were 150 mm × 50 mm × 8 mm, with a 2 mm square gap was between them, as shown in Figure 1a. QT S690 and MC S690 steels were considered for simulations to be carried out. Convection was applied on all surfaces of the plate except the heat-affected area. Figure 1 shows the FE model of the butt welded joint. Equation (7) could be resolved numerically with ANSYS® (19.2, ANSYS, Inc., Canonsburg, PA, USA) to carry out the sequential thermal distribution from the melting line to the base material. The geometry was divided into two parts with the characteristics described below.

The weld plate was made of two materials (QT S690 and TMCP S690), with a total of 148,147 and 30,300 nodes and elements, respectively. The weld bead was composed of 41,055 and 7800 knots and elements, respectively, which had a total of 189,202 and 38,100 individual nodes and elements, respectively. Figures 3 and 4 show the thermal conductivity and the specific heat as a function of the temperature of the high-strength steel QT S690/TMCP S690, respectively, and these values were obtained using the JMat software. This software was used to obtain the remaining thermo-mechanical material properties.

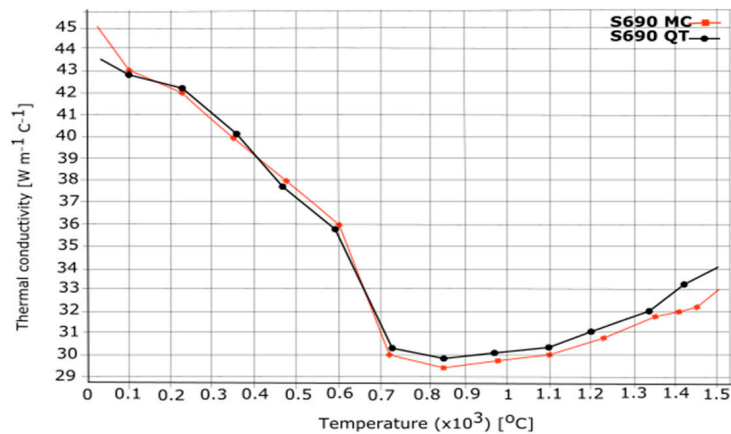


Figure 3. Thermal conductivity.

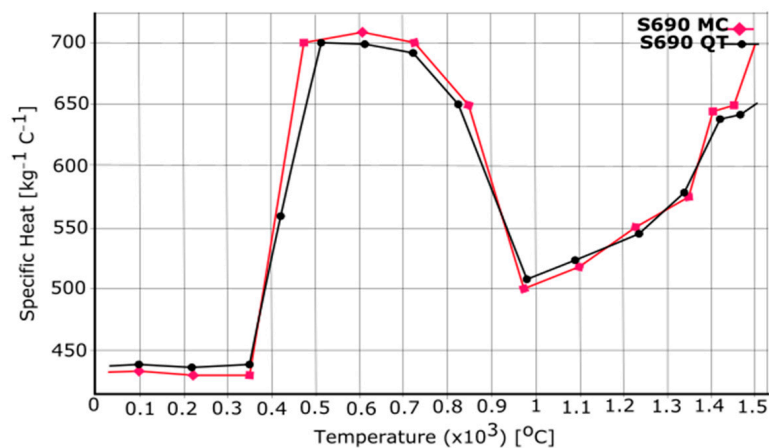
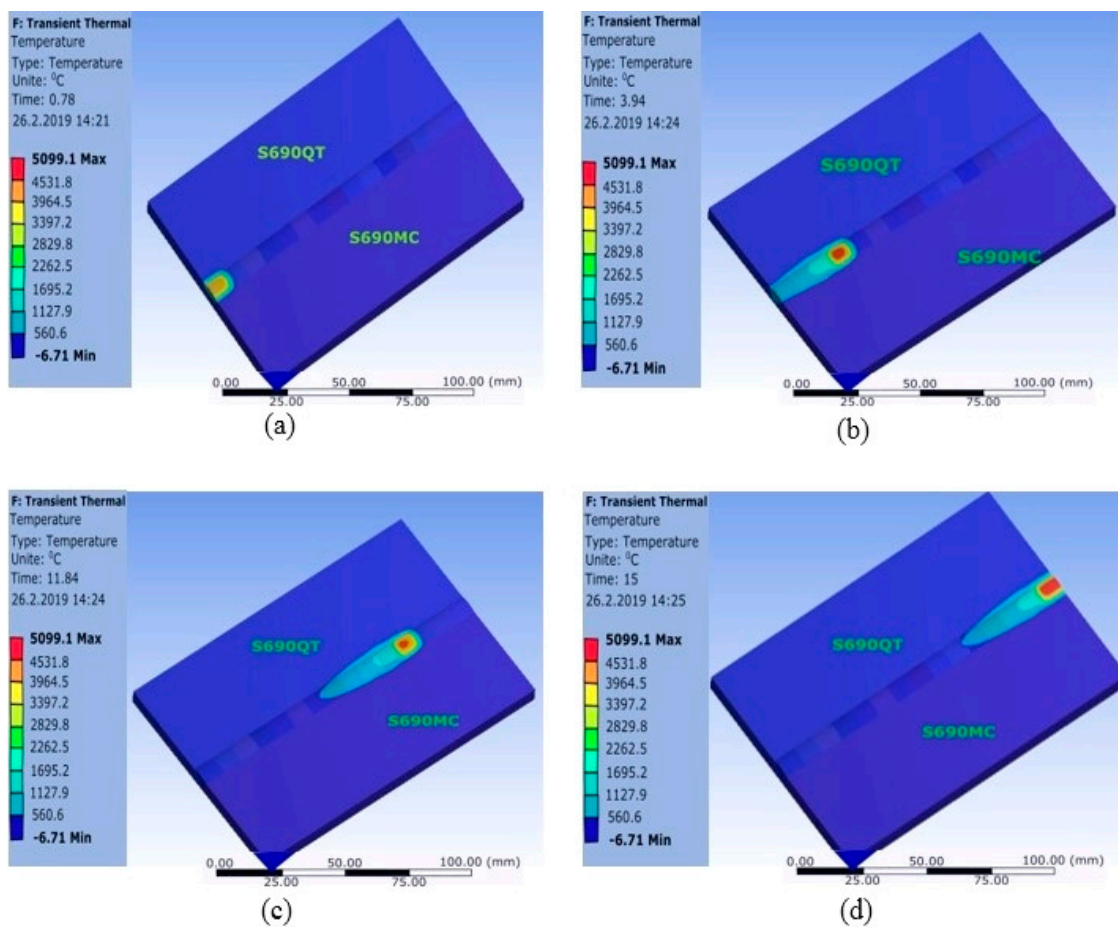


Figure 4. Specific heat.

#### 4. Results and Discussion

A heat input value was assigned step by step for the duration of the welding procedure at speeds of 27.18, 27.12, and 22.26 cm/min. Afterward, the different positions of the welding procedure were recorded. Figure 5a shows the beginning of the welding process, where the melting zone is shown in red, while Figure 5b shows the welding position after 15 s (one-third of the travel direction); we observed thermal diffusion from all sides of the materials and noted that this repair network was not uniform for both bodies of material. Figure 5c shows the welding position after 45 s (two-thirds of the travel direction), and Figure 5d illustrates the end of the weld after 60 s (the end of the travel direction). The total welding process lasted 46 s for the first welding process, 58 s for the second welding process, and 60 s for the third welding process.



**Figure 5.** Thermal simulation process: (a) starting process; (b) simulation after 15 s; (c) simulation after 45 s; (d) the end of the process after 60 s.

##### 4.1. Thermal Variations

Figure 6a–c shows the numerical results of the heat transfers in the weld seams of the two materials. The values of heat source applied to this program were 10, 14, and 17 kJ/cm. Subsequently, the same heat source values were experimentally applied using GMA welding as shown in Table 3. The analysis was carried out on the second welding pass. The first step was considered constant in all three samples. After welding the first pass, the weld joints underwent a slow cooling before applying the second-pass weld. Figures 6d and 7a,b represent the results of the temperature transfer from the melting point to the base material, allowing the evaluation of the required cooling time for the two base materials. On average, 1450 measurement points were recorded for each numerical and experimental analysis process. The analyses of the different behaviors of the heat sources led

to the ability to compare their behaviors. Figure 7c–e interpret the results of different heat sources (numerical and experimental) for each material. It was found that, when a heat source of 10 kJ/cm was applied, the numerical results indicated that the maximum measured temperatures in the QT steel and TMCP steel were approximately 1320 and 1200 °C, respectively, at a distance of 7 mm away from the centerline of the weld. The average cooling time of the two base materials was 14.5 s. During the experimental process, the average value of cooling time was 18.84 s. For the second test using heat input with a value of 14 kJ/cm, the numerical results indicated that the maximum temperatures in the QT steel and TMCP steel were approximately 1400 and 1300 °C, respectively, at a distance of 7 mm away from the centerline of the weld. The respective numerical and experimental cooling time results gave 24.85 and 30.45 s. For the last analysis using heat input with a value of 17 kJ/cm, the numerical results indicated that the maximum measured temperatures in the QT steel and TMCP steel were about 1600 and 1450 °C, with average values of the respective numerical and experimental cooling times of 29.45 and 36 s.

This difference in cooling time had an impact on the mechanical characteristics of the applied weld joint. An analysis of the samples in terms of the hardness and microstructure behavior allows us to understand in detail the implications of these cooling times.

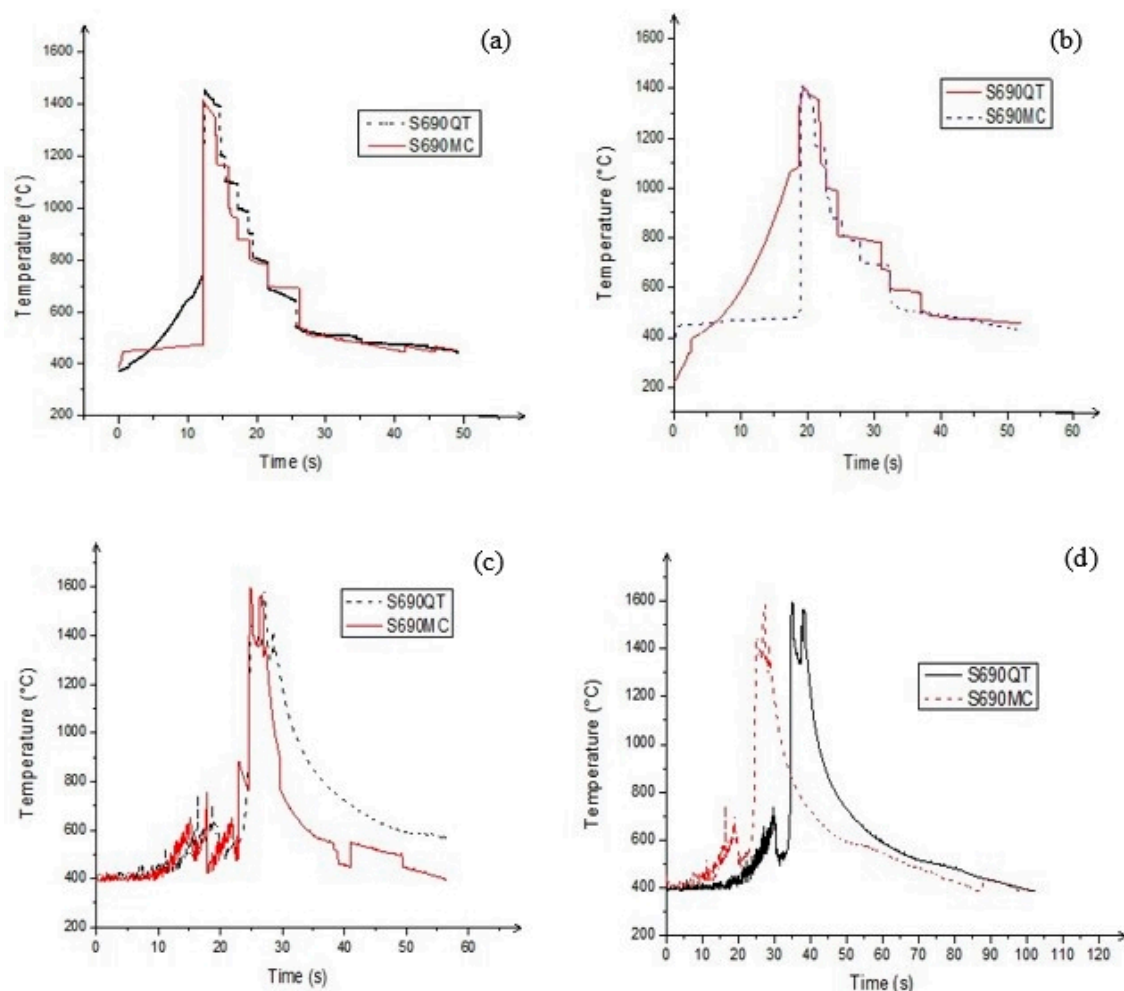


**Figure 6.** Cooling time results in the weld joint: numerical values using (a) 10 kJ/cm of heat input, (b) 14 kJ/cm of heat input, and (c) 17 kJ/cm of heat input; (d) experimental values using 10 kJ/cm of heat input.

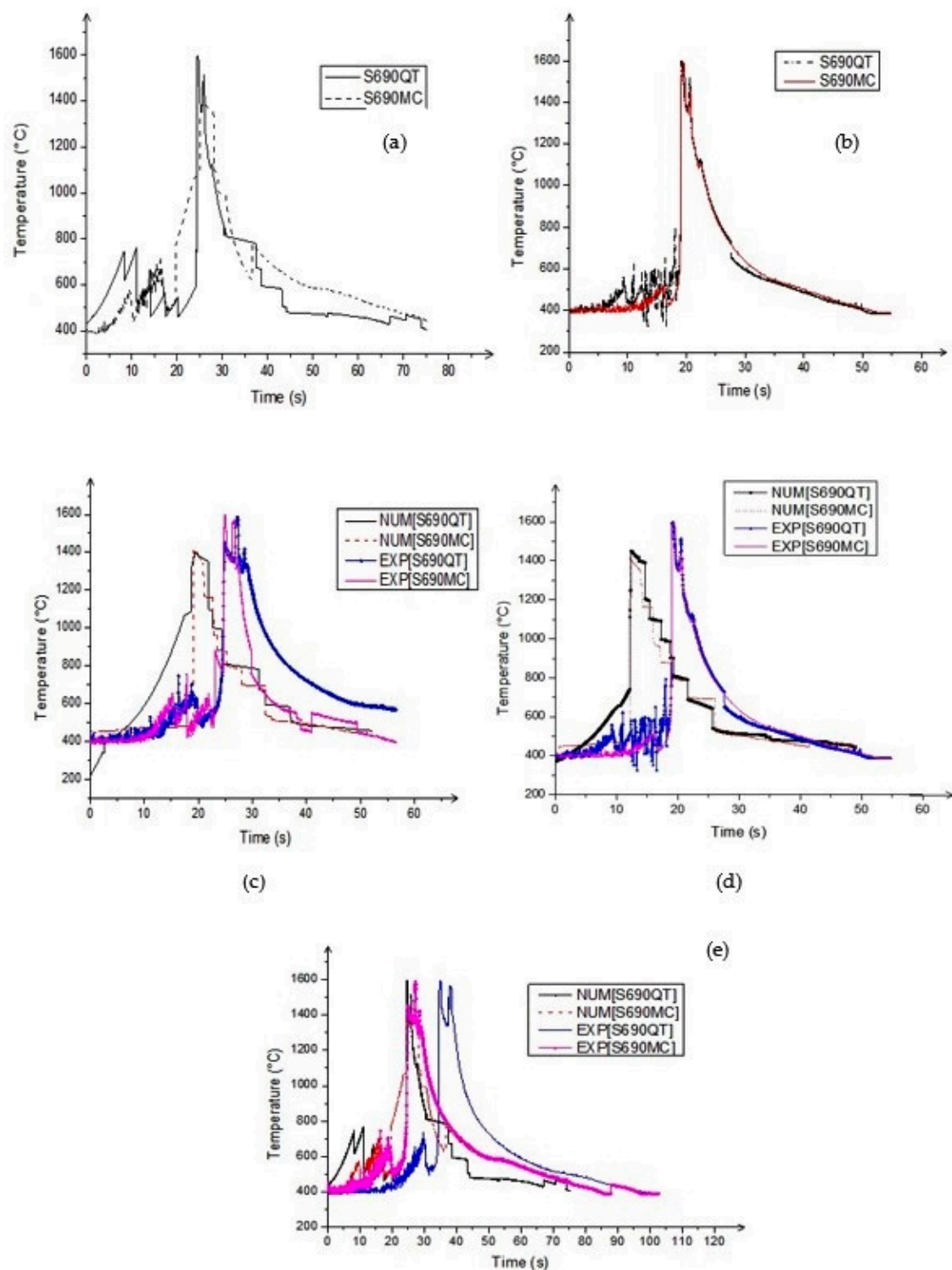


**Figure 7.** Cooling time results in the weld joint: experimental values using (a) 10 kJ/cm of heat input, and (b) 14 kJ/cm of heat input. Comparison between numerical and experimental values using (c) 10 kJ/cm of heat input, (d) 14 kJ/cm of heat input, and (e) 17 kJ/cm of heat input.

#### 4.2. Microstructure Behavior of the QT Steel Welded Joint

In the QT steel, the CGHAZ, FGHAZ, inter-critical HAZ (ICHAZ), and subcritical HAZ (SCHAZ) were defined by optical microscopy (Figure 8). The microstructure varied continuously with a local peak temperature. The typical optical microstructure of QT steel, consisting mainly of tempered martensite

and bainite, is shown in Figure 8a. In this figure, the size of the initial austenite grain corresponds to grain size 12 (5.6  $\mu\text{m}$ ) according to ASTM E112-13. The microstructure of the base metal is homogeneous, and in-equigranularity is not observed. A limited carbon content of up to 0.15% in the base metal allowed lath martensite to be obtained and the formation of twinned martensite to be prevented.

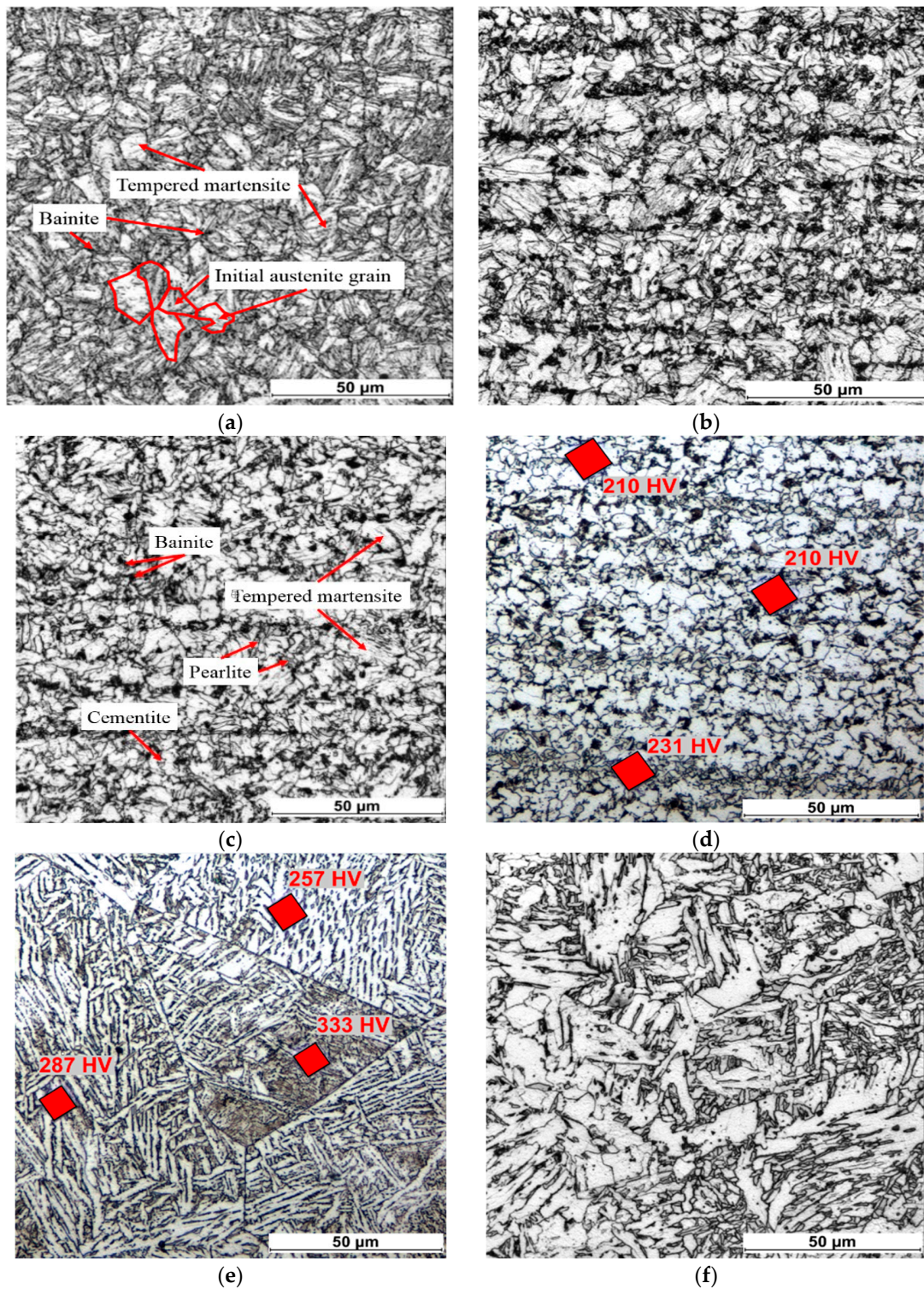


**Figure 8.** The optical microstructure of the quenched and tempered (QT) steel welded joint (second welding condition): (a) base metal; (b) subcritical heat-affected zone (SCHAZ); (c) inter-critical HAZ (ICHAZ); (d) fine-grain HAZ (FGHAZ); (e) coarse-grain HAZ (CGHAZ); (f) weld interface.

SCHAZ was the area most affected by the sudden changes in temperature, leading to the formation of cementite grains. In Figure 8b, we can identify some grain bainite grains of black cementite particles at this location, caused by carbide diffusion at low temperatures. The IGHZ corresponds to an area having a temperature range from the lower to upper critical point, and between the upper and lower critical point (cooling phase). During the heating phase, there was a temperature variation of about 720 to 910 °C in the HAZ. There was a transformation in grain austenite, which increased up to the peak temperature. During the cooling time, a transformation occurred in the first partial time of austenite grain (temperature ranging from 910 to 720 °C). At less than 720 °C, the solidification phase began with a transformation of small grain into a microstructure with a mixture of bainite, martensite (tempered), pearlite, and some cementite.

The FGHAZ refers to the HAZ which was subjected to peak temperatures between the upper critical point  $AC_3$  and the austenite grain coarsening temperature, typically between about 910 and 1300 °C (Figure 8d). The CGHAZ and FGHAZ are both zones that became fully austenitic due to the thermal weld cycle. After a  $\gamma \rightarrow \alpha$  transformation, the microstructure of these zones changed progressively depending on the previous austenite grain size. To identify and locate the CGHAZ and FGHAZ regions, it was necessary to rely on the different temperature ranges, or on the grain sizes in micrograph picture. During the heating phase (ferrite grain  $\alpha$  to austenite grain  $\gamma$ ), the grain surfaces grew (austenite grain increases). This development was possible due to the dissolution of the cementite, increasing the temperature. If the peak temperature decreased in this phase, there would have been a reduction in the growth of the original grain, which may have resulted in increased nitride and carbide formation. The microstructure of the CGHAZ of the QT steel in this work was composed of bainite and lath martensite (Figure 8e). Austenite grains grew during welding heating from 5.6  $\mu\text{m}$  (grain size 12 according to ASTM E112-13) (base metal) to 75  $\mu\text{m}$  (grain size 4–5). During the cooling phase (austenite  $\gamma$  to ferrite  $\alpha$  transformation), the large transforming grains broke down to form fine grains at temperatures around 720 °C. In the analysis of this microstructure, we can clearly identify two main grains: bainite and martensite (with low carbon). Bainite is identified at a higher temperature compared to martensite. This grain may have the appearance of a trace of ferrite grain and cementite ( $\text{Fe}_3\text{O}$ ), due to the high temperature of the upper bainite. The same traces of ferrite can be identified inside martensite grain at low temperatures.

The FGHAZ had the most reasonable grain structure. For the QT steel in this study, quantifying microstructural grain in the FGHAZ could help predict the possibility of brittle formations inside the microstructure. ImageJ 1.52p 22 software was used to define the different grain sizes in the microstructure. The measurement was made automatically with the aid of the ImageJ color threshold (Figure 9a,b). In total, 143 grains were counted from a surface sample with dimensions of 262  $\mu\text{m} \times 284 \mu\text{m}$ . The surfaces of each grain were measured, which gave the following results: with QT 690 steel, the smallest size evaluated was 1.3  $\mu\text{m}^2$ , and the maximum size was equal to 62  $\mu\text{m}^2$ . The general average value of the area was evaluated by applying the relationship where  $\bar{X}$  represented the general average,  $X_i$  is the measurement of grain size, and  $n$  is the number of grain sizes. The general average grain size value gave results of  $\bar{X} = 12.72 \mu\text{m}^2$ . The standard deviation (SD) of individual measurements was calculated using the relationship below; after all calculations, the value of SD was determined as 13.5  $\mu\text{m}^2$ .

The characterization of samples using the software makes it possible to compare the sizes of the grain sizes according to ASTM E112-13. At the FGHAZ, the average found was 12.72  $\mu\text{m}^2$ .

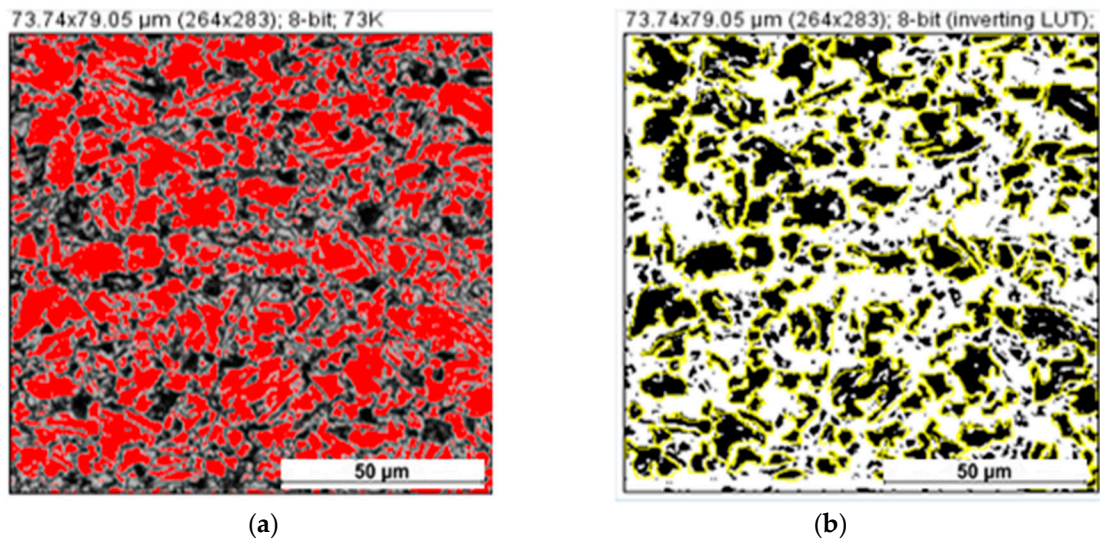


**Figure 9.** The microstructure of the FGHAZ region of QT steel for the second welded condition: (a) calibration using Threshold ImageJ; (b) measurement of grain area using ImageJ 1.52p 22.

#### 4.3. Microstructure Behavior of the TMCP Steel Welded Joint

The TMCP steel in this study was a high-strength low-alloy structural steel manufactured by thermo-mechanically controlled processing. The TMCP steel contained about 0.05% less carbon than the QT-steel (Table 1). The reduction in carbon content allowed considerable improvement in the low-temperature toughness of the base metal. The 690 TMCP steel was mainly composed of 70% bainite and 30% ferrite (Figure 10a). The size of the grains corresponded to ASTM 112-13 grain size 14 (3.0  $\mu\text{m}$ ). During the thermal transformation process, the CGHAZ was transformed in its first phase according to the bainite–ferrite morphology (B–F), with a small amount of martensite–austenite (M–A). During the cooling phase, the austenite grain was transformed into ferrite at a high temperature of 720  $^{\circ}\text{C}$ , and then into bainite. The internal composition of bainite may have retained some ferrite and carbide due to the elevation of temperature in this area. In the micrographs, most prior austenite grain boundaries are visible, allowing the mean austenite grain size to be measured. The ICHAZ and SCHAZ regions of the TMCP steel can hardly be distinguished (Figure 10d,e). The reason for this view was the low carbon content in the TMCP steel, which meant that heating to temperatures around the critical point  $AC_1$  did not produce large-scale nucleation of cementite and its coagulation.

The same measurement procedure as with the QT steel was also followed with the TMCP steel (Figure 11a,b), with a total grain number count of 143 grains. It was observed that the smallest grain size evaluated was 1  $\mu\text{m}^2$ , and the maximum grain size was equal to 37  $\mu\text{m}^2$ . Based on these values, the overall value of the size was evaluated at  $\bar{X} = 7.6 \mu\text{m}^2$ . The standard value of grain deviation was calculated as 5.8  $\mu\text{m}^2$  (ASTM E112-13).

The average austenite grain size was 89.0  $\mu\text{m}^2$  (ASTM E112-13 grain size 4). Within the prior austenite grain, several crystallographic packets could be identified, with high misorientation angles between them, which slightly refined the effective grain size. The ratio of grain size number to grain size area of the TMCP steel, which was done to evaluate the surface concentration in the FGHAZ, is presented in Figure 12a. The result shows that, for the total of 143 grains, a higher grain concentration in the interval from 1–10  $\mu\text{m}^2$  was occupied by 112 grains. The remainder of the grains (31) occupied the surface area in the range from 10–25  $\mu\text{m}^2$ . In Figure 12b, the statistical data present the results of QT steel grain size by sample; 80 grains were identified occupying an area of 1–10  $\mu\text{m}^2$ , while the second zone included 35 grains occupying an area of 10–30  $\mu\text{m}^2$ , and the last zone included 28 grains occupying an area of 30–62  $\mu\text{m}^2$ .

Comparative analysis indicates a high concentration of grains in the upper surfaces of the QT 690 compared to the TMCP 690 steel. The average difference was  $12.7 \mu\text{m}^2$  for QT 690 and  $7.6 \mu\text{m}^2$  for TMCP 690 steel.

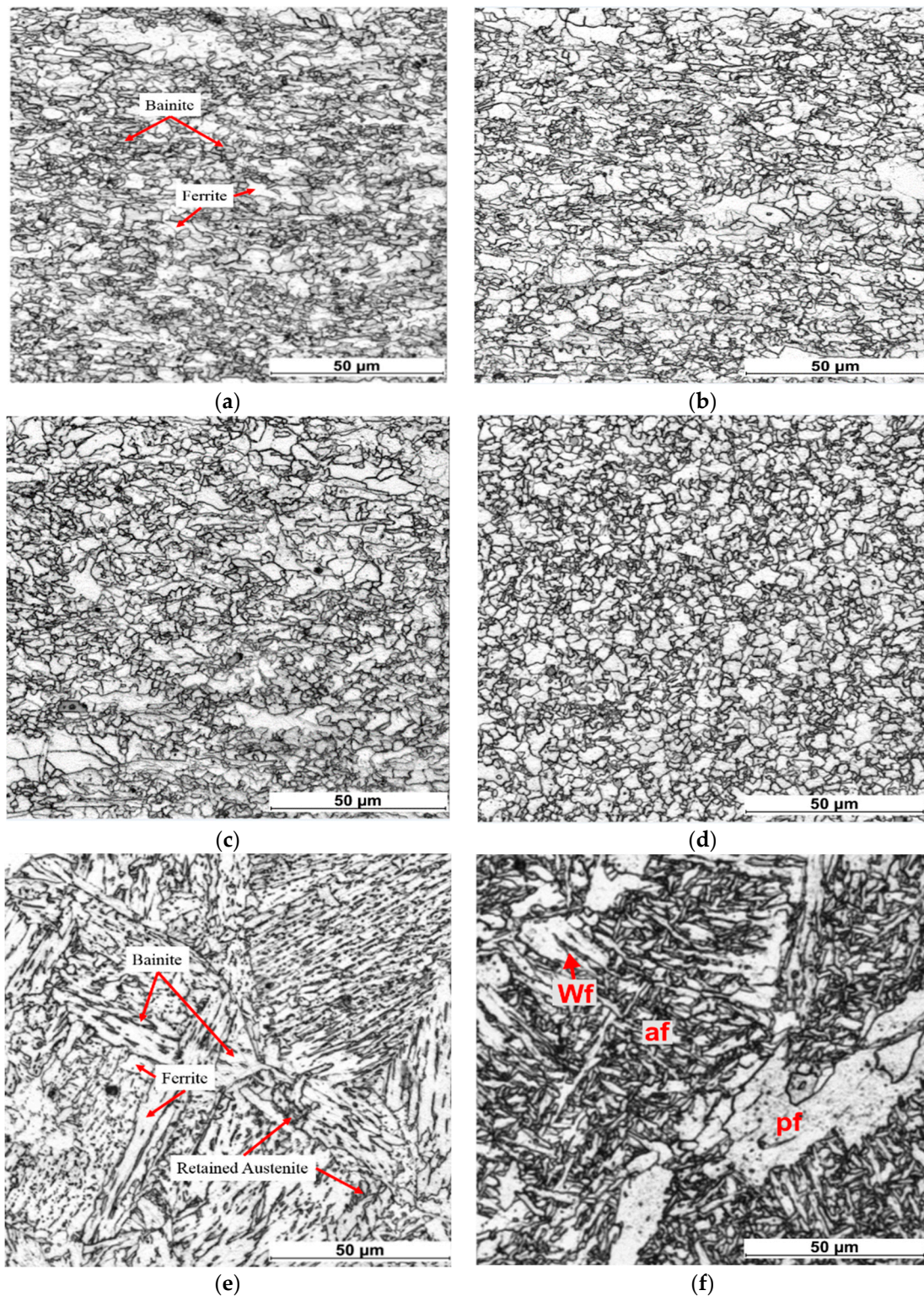


**Figure 10.** The microstructure of the thermo-mechanically controlled process (TMCP) steel welded joint with the second welding condition: (a) base metal; (b) SCHAZ; (c) ICHAZ; (d) FGHAZ; (e) CGHAZ; (f) weld metal (Wf—Widmanstätten ferrite; af—acicular ferrite; pf—polygonal ferrite).

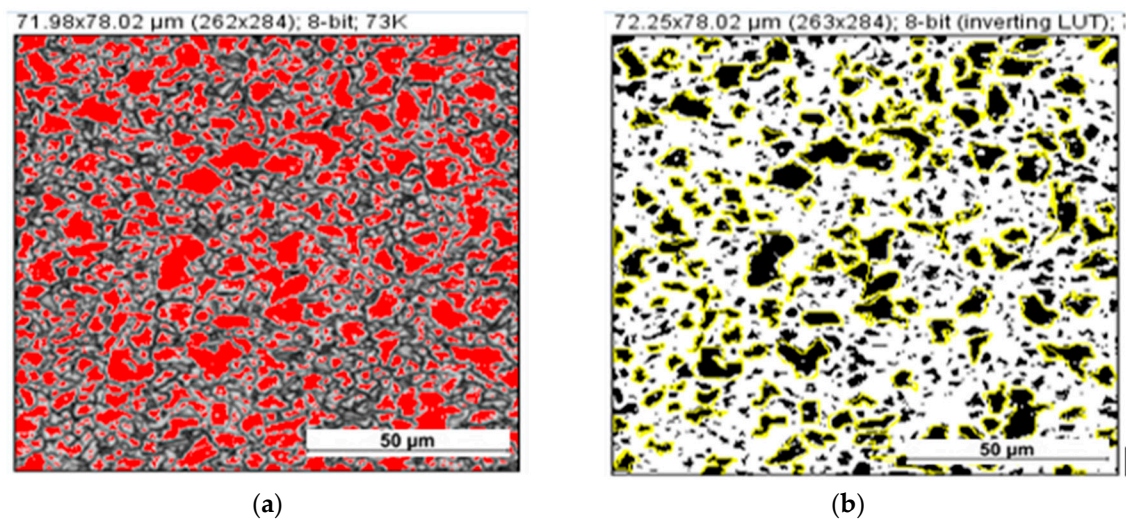


**Figure 11.** The microstructure of the FGHAZ region of TMCP steel for the second welding condition: (a) calibration using Threshold ImageJ; (b) measurement of grain area using ImageJ 1.52p 22.

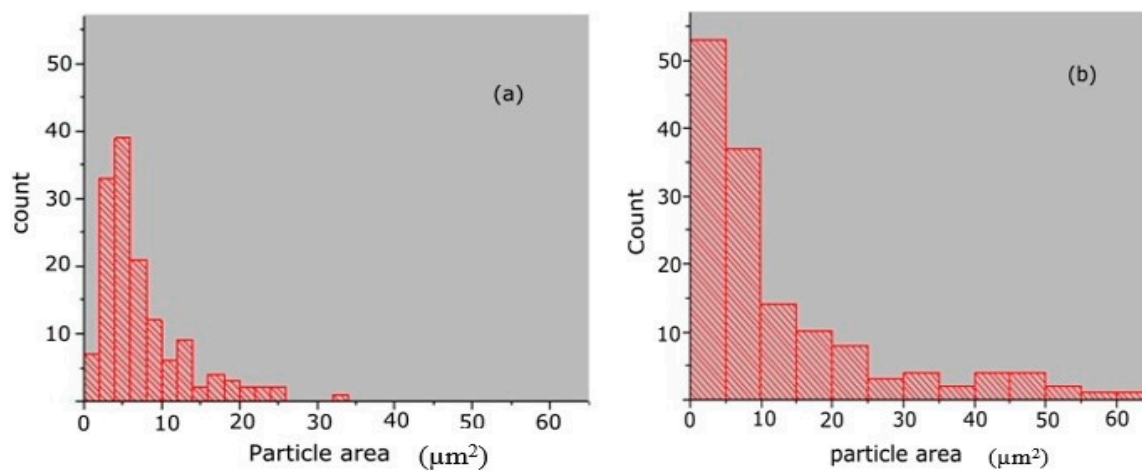


**Figure 12.** Ratio of grain number (count) to particle area: (a) for TMCP steel; (b) for QT steel.

#### 4.4. The Microstructure of the Weld Metal

During the welding process of the different samples, the zone in which the filler metal is applied is generally subjected to the highest temperatures. In the analysis of the different samples, a formation was observed as a function of the temperature phases: Widmanstätten, polygonal, and acicular ferrite. It should be noted here that these forms of ferrite differ in their internal displacement, and at the boundary of the austenite grains. During the cooling process (from  $\gamma$  to ferrite  $\alpha$  transformation), polygonal ferrite was formed. A longer cooling time led to the formation of Widmanstätten ferrite. Its development can be seen at the boundary of austenite grain during the carbon diffusion. When the temperature decreased, there was the formation of an acicular ferrite transformation. It should be noted that acicular ferrite occurs within small grains during carbon diffusion and during equilibrium nucleation. The difference is that, with acicular ferrite, there is no diffusion during growth.

#### 4.5. Comparison of Dissimilar Weld Joint Hardness Profiles

The experimental data show that the HAZ of the same grade steels with different chemical composition and initial microstructure was significantly different for the same welding conditions. Naturally, the local mechanical properties of the HAZ and, consequently, the mechanical properties of the weld joints would also be substantially different. The hardness measurements made in this

analysis were for one line per sample. Three samples were measured (for 10 kJ/cm, 14 kJ/cm, and 17 kJ/cm). Figure 13 shows the heterogeneity of the welded joints. The hardness of the weld metal was also virtually identical (220 vs. 230 HV0.1). The weld metal was undermatched, and the yield stress of the filler metal was 72% of that of the base metal. When the heat source value was applied at 10 kJ/cm, the hardness value on the CGHAZ increased by 15% to 310 HV0.1 vs. 270 HV0.1 of the hardness of the base material, and decreased by 10% to 260 vs. 290 HV0.1 for the TMCP steel. Upon increasing heat input from 1 to 10 to 17 kJ/cm, the cooling time increased, and the hardness of the CGHAZ in the QT steel decreased from 310 to 260 HV0.1. In the FGHAZ, the hardness of the two steels underwent the greatest decrease—20% for the QT steel, and 30% for the TMCP steel. The hardness of the metal heated slightly below  $AC_3$  decreased by 30% to 210 HV0.1 (ICHAZ). Upon heating between  $AC_1$  and  $AC_3$  (ICHAZ), the three heat source values resulted in an average hardness value of 210 HV0.1 for the QT steel and 230 HV0.1 for the TMCP steel. The cause of the austenite composition in the microstructure varying from 0 to 100% depended on the local peak temperature. As the austenite transforms into ferrite during cooling, its fraction determines the hardness at the inter-critical HAZ region. The SCHAZ area was much more impacted, with a meager hardness value of 180 HV0.1 when the heat source was high (17 kJ/cm). For the TMCP steel, the average value of 260 HV0.1 was reasonable.

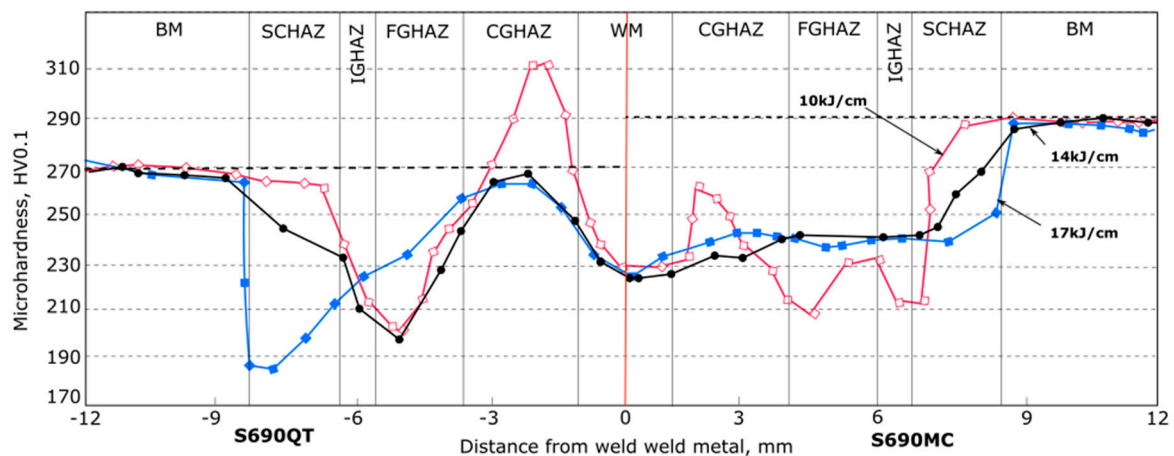


**Figure 13.** Effect of heat input on the microhardness profile of the welded joints: (left) QT steel; (right) TMCP steel. The dotted line shows the base metal hardness.

The width of the soft (unhardened) zone was different in both plates of steel; in the QT steel, it was mainly determined by the width of the fine-grain region, and, in the TMCP steel, it was determined by the total width of the coarse- and fine-grain regions. In the latter case, the width of the soft zone was equal to 5 mm, which is large relative to the thickness of the welded joint. The sharp increase in hardness can be explained by the formation of a bainitic–martensitic microstructure (due to the high carbon content) and grain growth. In the second case, the hardness drop was caused by primary recrystallization of the microstructure and the formation of more equilibrium products of austenite decomposition during cooling. Both plates of steel showed the lowest hardness in the fine-grain region due to the creation of predominantly polygonal ferrite.

## 5. Conclusions

This numerical and experimental investigation focused on the analysis of the effect of heat input on the microstructure and mechanical properties of weld joints of 690-MPa QT and TMCP steel. Based on the results of this study, the analysis of these heat inputs focused on two HAZ regions: the CGHAZ and FGHAZ. The key findings can be summarized as follows:

1. For developing the numerical analysis, a three-dimensional (3D) nonlinear thermal analysis finite element model was used to predict the thermal fields during the welding. The results showed

an acceptable confirmation between the experimental and numerical thermal fields of the three samples within a range of 7–19% in predicting the temperature.

2. The maximum respective values of the temperature measured in QT steel and TMCP steel were about 1300 and 1200 °C for a heat input of 10 kJ/cm, 1400 and 1300 °C for a heat input of 14 kJ/cm, and 1600 and 1450 °C for a heat input of 17 kJ/cm.
3. A heat input of 10 kJ/cm resulted in the maximum rapid cooling time (numerical  $t_{8/5}$ , 14.5 s, and experimental, 18.84 s), which increased hardness by 15% to 310 HV0.1 in the CGHAZ region of the QT steel and decreased the hardness value by 10% to 260 vs. 290 HV0.1 for the TMCP steel. In the QT steel, local brittle zone formations in the martensite–bainite microstructure in the CGHAZ were observed.
4. In the TMCP steel, the hardness drop was caused by a reconstructive transformation in the primary recrystallization of the microstructure and the formation of more equilibrium products of austenite decomposition (CGHAZ), with lowest hardness seen in the fine-grain heat-affected zone (FGHAZ) region due to the creation of polygonal ferrite.
5. Upon increasing heat input from 14 to 17 kJ/cm, the cooling time of the welding process was increased (numerical  $t_{8/5}$ , 29 s, and experimental, 36 s), leading to a decrease in the hardness of the CGHAZ in the QT steel by 16% from 310 to 260 HV0.1 due to the full austenite (thermal weld cycle), while maintaining the hardness value of the TMCP steel. This helped avoid the brittle formation in the inter-critical coarse-grain HAZ (ICCGHAZ) of TMCP steel and also to avoid defects in the weld zone.
6. In the FGHAZ, the hardness of the two steels underwent the greatest decrease—20% for the QT steel, and 30% for the TMCP steel.
7. The SCHAZ area was greatly impacted with a very low hardness value of 180 HV0.1 when the heat source was high (17 kJ/cm). The main reason for that softening was a high heat input; thus, heat input should be controlled and limited, especially for a thick plate, because the softening effect of the welded joint is proportional to the plate thickness.
8. The coarse-grain heat-affected zone (CGHAZ) showed relatively high hardness and large-size grains, and the tempering zone had comparable hardness and grain size to the base metal.
9. The analyzed grain samples showed an increased surface on the 690 QT steel (12.6  $\mu\text{m}^2$ ) compared to the 690 TMCP steel (4.43  $\mu\text{m}^2$ ). A probable reason is that the carbon content in QT steel, higher compared to 690 TMCP steel, caused carbon diffusion during para-equilibrium nucleation and growth in the austenite grain size.

The results obtained in this analysis may help predict the heat source values expected to have a favorable yield of material properties in the heat-affected zone. Future studies could be conducted to simulate and analyze the effect of the heat input on the mechanical behavior (stress and distortions) of the weld joint.

**Author Contributions:** F.N.B. performed the numerical and experiment analysis, wrote the original draft, and contributed to review and editing. P.K. supervised the study, reviewed the results, and wrote the conclusion. P.L. and V.K. provided the resources.

**Funding:** The research was funded by Energy-efficient systems based on renewable energy of Arctic conditions “EFREA”, Grant number K51054 and Finnish cultural foundation for its financial support.

**Acknowledgments:** The authors would like to thank Esa Hiltunen, Anti Heikkinen and Antti Kähkönen for their support to the arrangement of experimental work.

**Conflicts of Interest:** The authors declare no conflicts of interest.

## References

1. Haslberger, P.; Holly, S.; Ernst, W.; Schnitzer, R. Microstructure and mechanical properties of high-strength steel welding consumables with a minimum yield strength of 1100 MPa. *J. Mater. Sci.* **2018**, *53*, 6968–6979. [[CrossRef](#)]

2. Di, H.; Sun, Q.; Wang, X.; Li, J. Microstructure and properties in dissimilar/similar weld joints between DP780 and DP980 steels processed by fiber laser welding. *J. Mater. Sci. Technol.* **2017**, *33*, 1561–1571. [[CrossRef](#)]
3. Pandey, C.; Mahapatra, M.; Kumar, P.; Thakre, G.; Saini, N. Role of evolving microstructure on the mechanical behavior of P92 steel welded joint in as-welded and post weld heat treated state. *J. Mater. Proc. Technol.* **2019**, *263*, 241–255. [[CrossRef](#)]
4. Mironov, S.; Sato, Y.; Yoneyama, S.; Kokawa, H.; Fujii, T.; Hirano, S. Microstructure and tensile behavior of friction-stir welded TRIP steel. *Mater. Sci. Eng. A* **2018**, *717*, 26–33. [[CrossRef](#)]
5. Hulka, K.; Gray, J.M. High-temperature processing of line-pipe steels/niobium science and technology. In Proceedings of the International Symposium Niobium, Orlando, FL, USA, 2–5 December 2001.
6. Nishioka, K.; Ichikawa, K. Progress in thermomechanical control of steel plates and their commercialization. *Sci. Technol. Adv. Mater.* **2012**, *13*, 203001.
7. Hochhauser, F.; Ernest, W.; Rauch, R.; Vallant, R.; Enzinger, N. Influence of the soft zone on the strength of welded modern HSLA steels. *Weld. World* **2006**, *56*, 77–85. [[CrossRef](#)]
8. Kim, B.; Lee, S.; Kim, J.; Lee, D. Microstructure and local brittle zone phenomena in high-strength low-alloy steel welds. *Metall. Trans. A* **1999**, *22*, 139–149. [[CrossRef](#)]
9. Loureiro, R. Effect of heat input on plastic deformation of undermatched weld. *J. Mater. Proc. Technol.* **2002**, *128*, 240–249. [[CrossRef](#)]
10. Hwang, R.; Lee, T.; Lee, G. Correlation of microstructure and mechanical properties of thermo-mechanically processed low-carbon steels containing boron and copper. *Metall. Mater. Trans. A* **2010**, *41*, 85–96. [[CrossRef](#)]
11. Chang, W.S. Microstructure and mechanical properties of 780 MPa high strength steel produced by direct quenching and tempering process. *J. Mater. Sci.* **2002**, *37*, 1973–1979. [[CrossRef](#)]
12. Schroter, F. Structural steel for the application in offshore, wind and hydro energy production. Comparison of application and welding properties of frequently used materials. *Int. J. Microstruct. Mater. Prop.* **2011**, *6*, 4–19. [[CrossRef](#)]
13. Lambert-Perlade, A.; Gourgues, A.F.; Pineau, A. Austenite to bainite transformation in the heat-affected zone of a heat strength low carbon steel. *Acta Mater.* **2004**, *52*, 2337–2348. [[CrossRef](#)]
14. Lanberte-Perlade, A.; Gourgues, A.F.; Besson, J.; Sturel, T.; Pineau, A. Mechanism and modeling of cleavage fracture in simulated heat-affected zone microstructures of high-strength low alloy steel. *Metall. Mater. Trans. A* **2004**, *35*, 1039–1053. [[CrossRef](#)]
15. Bhatti, A.; Barsoum, Z.; Hidekazu, M.; Barsoum, I. Influence of thermo-mechanical material properties of different steel grades on welding residual stresses and angular distortion. *Mater. Des.* **2015**, *65*, 878–889. [[CrossRef](#)]
16. Liu, D.; Li, T.; Emi, T. Microstructure and mechanical properties in hot-rolled extra high-yield-strength steel plates for offshore structure and shipbuilding. *Metall. Mater. Trans. A* **2011**, *42*, 1349–1361. [[CrossRef](#)]
17. Layus, P.; Kah, P.; Ryabov, V.; Martikainen, J. Evaluation of applicability of thick E500 TMCP and F500W QT-steel plates for Artic service. *Int. J. Mech. Mater. Eng.* **2016**, *11*, 1–15. [[CrossRef](#)]
18. Dusan, A.; Vukic, L.; Ruzica, R.; Srbislav, A.; Branislav, H.; Milan, D. Optimal welding technology of high strength steel S690QL. *Mater. Eng.* **2015**, *22*, 33–47.
19. Porter, D.; Laukkanen, A.; Nevasmaa, P.; Rahka, K.; Wallin, K. Performance of TMCP-steel with respect to mechanical properties after cold forming and post-forming heat treatment. *Int. J. Press. Vessel. Pip.* **2004**, *81*, 867–877. [[CrossRef](#)]
20. Sadeghian, M.; Shamanian, M.; Shafyei, A. Effect of heat on microstructure and mechanical properties of dissimilar joints between super duplex stainless steel and high strength low alloy steel. *Mater. Des.* **2014**, *60*, 678–684. [[CrossRef](#)]
21. Ito, R.; Hiraoka, K.; Shiga, C. Characteristics of the heat-affected zone in ultra-fine-grained steel during ultra-narrow gap GMA welding. *Weld. Int.* **2005**, *19*, 458–466. [[CrossRef](#)]
22. Hamada, M. Control of strength and toughness at the heat affected zone. *Weld. Int.* **2003**, *17*, 265–270. [[CrossRef](#)]
23. Pirinen, M.; Martikainen, J.; Layus, P.; Karhin, V.; Ivanov, Y.S. Effect of heat input on the mechanical properties of welded joints in high-strength steel. *Weld. Int.* **2015**, *2*, 14–17. [[CrossRef](#)]
24. Lan, L.; Qiu, C.; Zhao, D.; Gao, X.; Du, L. Microstructural characteristics and toughness of the simulated coarse-grained heat affected zone of high strength low carbon bainite steel. *Mater. Sci. Eng. A* **2011**, *529*, 192–200. [[CrossRef](#)]

25. Shi, Y.; Han, Z. Effect of thermal weld cycle on microstructure and fracture toughness of simulated heat-affected zone for an 800 MPa grade high strength low alloy steel. *J. Mater. Proc. Technol.* **2008**, *207*, 30–39. [[CrossRef](#)]
26. Goldack, J.; Chkravarti, A.; Bibby, M. A new finite element model for welding heat sources. *Metall. Trans. B* **1984**, *15*, 299–305. [[CrossRef](#)]



© 2019 by the authors. Licensee MDPI, Basel, Switzerland. This article is an open access article distributed under the terms and conditions of the Creative Commons Attribution (CC BY) license (<http://creativecommons.org/licenses/by/4.0/>).